ACS NANO

www.acsnano.org

ARTICLE

Defect Self-Elimination in Nanocube Superlattices Through the Interplay of Brownian, van der Waals, and Ligand-Based Forces and Torques

Jaewon Lee,◆ Zexi Lu,◆ Zhigang Wu,◆ Colin Ophus, Gregory K. Schenter, James J. De Yoreo, Jaehun Chun,* and Dongsheng Li*

Cite This: *ACS Nano* 2024, 18, 32386–32400

Read Online

ACCESS | Metrics & More | Article Recommendations | Supporting Information

ABSTRACT: **Understanding defect healing is necessary to control the electronic and optoelectronic performance of devices based on nanoparticle (NP) superlattices. However, a key challenge remains to understand how NP interactions and the resulting dynamics are coupled to defect self-elimination during assembly processes. Additional degrees of freedom that account for the anisotropic nature of NPs associated with rotational dynamics and torques further complicate the challenge. Here, we investigate nanocube (NC) superlattices by employing liquid-phase transmission electron microscopy, continuum theory, and molecular dynamics simulations. Our detailed analyses reveal that interparticle forces and torques due to ligand interactions dominate those from Brownian motions and van der Waals interactions. More importantly, NC translations and rotations induced by unbalanced forces and torques are transmitted to neighboring NCs, prompting "chain interactions" in a two-dimensional (2D) network and expediting self-elimination. The mechanistic understanding will further enable the design and fabrication of defect-free superlattices as well as those with tailored defects via assembly of anisotropic particles.**

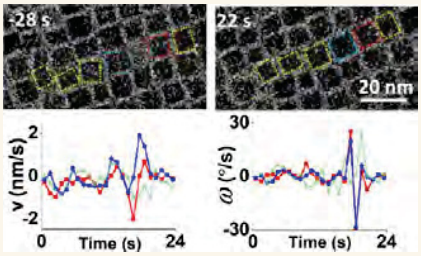

KEYWORDS: *collective dynamics, superlattices, defect self-elimination, in situ liquid cell TEM, anisotropic particles, interplay of forces and torques*

1. INTRODUCTION

NP superlattices formed via self-assembly have emerged as promising platforms for fabricating electronic and optoelectronic devices with superior performance.[1] Various bottom-up methods, such as casting,[2,3] dip-coating,[4,5] doctor blading,[6,7] and Langmuir–Blodgett deposition,[8,9] have been developed. However, defect generation is inevitable and difficult to control regardless of the method.[1,10] One of the important reasons these defects arise originates from nonuniform NP sizes and morphologies. In addition, aggregation of small clusters of NPs in solutions or slurries during assembly processes can introduce defects due to a misaligned or imperfectly matched lattice between clusters.[1,10,11] Although various post-treatment methods, such as thermal annealing, solvent annealing, and exposure to electric fields, promote defect healing, precise control of the defects has not been reported in literature due to a lack of understanding of NP healing mechanisms.[12−14]

Microstructures of the superlattice, analogous to lattice structures of molecular crystals, are decisive factors in determining the free energy of an overall superlattice system; various types of defects, such as vacancies and dislocations, in the superlattices can lead to multiple degeneracies and metastable states of the system. Defect elimination decreases the free energy of the superlattice. In defective regions, unbalanced van der Waals (vdW) and ligand interactions, along with random Brownian motions on NPs, can constantly disturb NP positions, drive perpetual migration, and lower the free energy of the superlattice. The interplay between colloidal interactions (i.e., energetics) and hydrodynamics (i.e., dynamics of particle motions) is expected to play a critical role in determining superlattice structures. Therefore, coupling energetic driving forces to the dynamic response is necessary to understand any mechanism of defect healing in superlattices.

Received: September 9, 2023
Revised: September 30, 2024
Accepted: October 16, 2024
Published: November 11, 2024

https://doi.org/10.1021/acsnano.3c08610
ACS Nano 2024, 18, 32386–32400

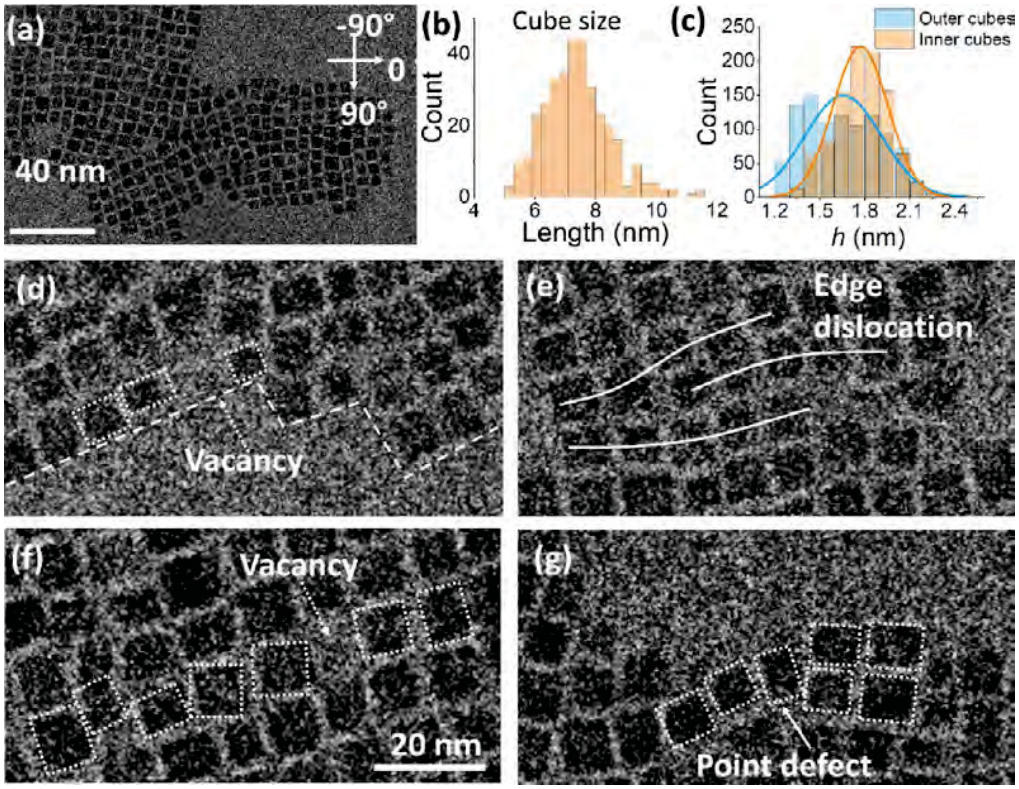

Figure 1. Observations of NC assembly with defects in superlattice and calculated forces and torques. (a) A representative image from *in situ* LP-TEM Movie S1 (46.1s). (b) Particle size distribution of the NCs in (a). (c) Measured separation (h) and distributions of the inner and outer NCs of the superlattice at 6.1 16.1, 26.1, 36.1, 46.1, 56.1, 66.1, 76.1, 86.1, and 96.1 s of the in situ LP-TEM Movie S1. (d–g) TEM images showing vacancy, point, and edge-dislocation defects, respectively.

The coupling becomes more intricate due to anisotropic shapes that can impose additional complexity such as torque (i.e., orientation-dependent interaction) and resulting rotation.[11,15,16] Unlike isotropic spherical NPs, cubic or cuboidal particles with nonuniform sizes and shapes introduce a large variety of separation distances between particle surfaces.[17] Nakouzi et al. demonstrated that the rhombohedral shape of boehmite crystals induces translational and rotational motions via the coupling of orientation-dependent colloidal dispersion forces and hydrodynamic mobilities.[18]

Because of the lack of efficient mathematical formulations for interactions between nonspherical shaped NPs, many previous studies have used scaling arguments to understand the vdW, ligand, and Brownian forces/torques among NPs based on limited configurations (e.g., face–face and edge–edge configurations for rhombohedral particles). For example, Xiao et al. explained the oriented attachment (OA) processes of Ag NCs only based on the face-to-face configurations.[19] Alternatively, some studies used molecular dynamics (MD) simulations or theoretical models based on a spherical approximation.[20] However, MD simulations typically present dynamics of a limited number of NPs over a few nanoseconds due to computational cost, or they are inherently limited in their ability to implement many-body contributions for vdW interactions between NPs.[21−24] The theoretical models for NPs based on spherical shapes fail to describe colloidal interactions at short-separation distances where the shape-dependent nature of interactions plays a significant role.[18] Therefore, a full mechanistic understanding has not been achieved, especially regarding the interplay between colloidal interactions and hydrodynamics, despite extensive theoretical,[25−30] and experimental[16,27,31−36] studies on self-assembly of anisotropic NPs. To address this challenge, a combination of complementary schemes covering spatial and temporal scales of interest and incorporating the distinctive nature of anisotropic NPs is required (for example, MD simulation insights into the dynamics and conformation of ligand-coated nanocrystals[21,22] and a theoretical model based on nonspherical colloidal interactions to describe long-range interactions).[37,38]

In this study, we investigated the self-assembly and subsequent defect healing of cuboidal palladium (Pd) NC superlattices by coupling experimental observations from *in situ* liquid-phase transmission electron microscopy (LP-TEM) with theoretical/MD modeling. We developed and implemented models of force and torque (i.e., vdW force and torque [F_{vdW} and τ_{vdW}], steric hindrance force and torque [F_{Sh} and τ_{Sh}], and Brownian force and torque [F_{Br} and τ_{Br}]) to obtain quantitative understanding of observed translational and rotational motions of cubic or cuboidal NPs that drive the elimination of point, vacancy, and edge-dislocation defects. Here, a point defect refers to an extra particle in the lattice. Classical MD based on well-documented force fields is further considered to rigorously understand the dominant driving forces behind the NP motions from an atomistic perspective by implementing the detailed conformation of ligands that cannot be captured by theoretical models alone.

https://doi.org/10.1021/acsnano.3c08610
ACS Nano 2024, 18, 32386−32400

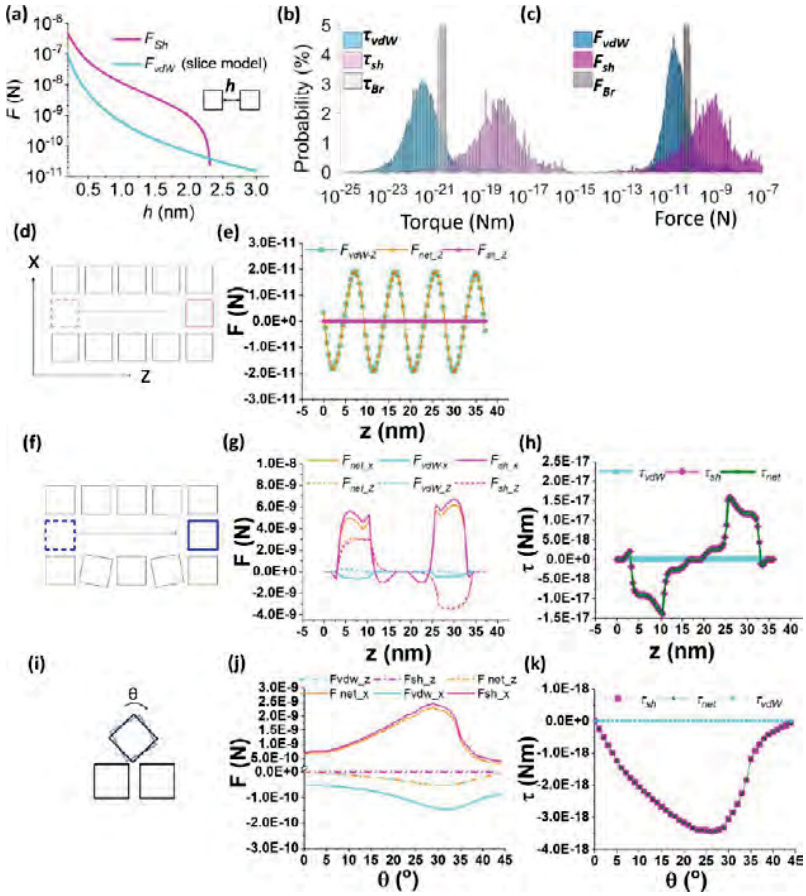

Figure 2. Calculated forces and torques for experiments and three representative configurations. (a) Theoretical calculation of F_{vdW} and F_{Sh} between two face-to-face NCs (7.5 × 7.5 × 7.5 nm) as a function of h. (b) Calculated τ_{vdW}, τ_{Sh}, and τ_{Br} and (c) F_{vdW}, F_{Sh}, and F_{Br} on all NCs observed by *in situ* LP-TEM over time after attaching two clusters in Movie S1. (d, f, and i)) Configurations of assembled NCs. The pink and blue NCs in (d) and (f), respectively, migrate from the dotted position to the solid lined position. The second and fourth NCs in the bottom layer in (f) are rotated by 20° and −20° respectively. The upper NC in (i) rotates clockwise. (e) The forces acting on the pink NC in (d) as a function of the position in the z-direction. (g) The forces and (h) torques acting on the blue NC in (f) as a function of position in the z-direction. (j) The forces and (k) torques acting on the upper NC in (i) as a function of θ. Cube dimensions are 7.5 × 7.5 × 7.5 nm with an h of 2.5 nm.

2. RESULTS AND DISCUSSION

2.1. LP-TEM Observation of NC Motions and Defect Elimination in Superlattices. Our synthesis (see Methods section) yields monodisperse Pd cubes and cuboids coated by 1-dodecanethiol with an average size of ∼7.5 nm (Figure 1a,b). We use the term nanocube (NC) to represent both true cubes and cuboidal nanoparticles in this paper. Through *in situ* LP-TEM experiments (toluene as the solvent; see Methods section), we observe that Pd NCs assemble into 2D superlattices (Movie S1), with one layer of NCs in a square pattern on the Si_xN_y membrane of the liquid cell. Occasionally, we find a few NCs on top of the 2D superlattices. The clusters are in a dynamic form with translational and rotational motions of both "inner" and "outer" NCs. The interparticle separation (h) fluctuates, ranging primarily from 1.2 to 2.4 nm with an average of ∼1.7 nm (Figure 1c). The van der Waals forces (F_{vdW}) acting on the inner NCs are canceled out to some extent by opposite neighbors—thus, F_{vdW} is smaller than that acting on the outer NCs, leading to a slightly larger h between the inner NCs than between the outer NCs (Figure 1c). The unconfined outer NCs on the peripheral boundary of the cluster move significantly faster (up to ∼100 nm/s) than those inside the cluster (up to ∼2 nm/s), whose motion is hindered by their neighbors. The rapid movement of the outer NCs can lead to formation of defects, such as a vacancy on the peripheral boundary (Figure 1d). Cluster attachments can also introduce defects, creating an extra lattice line (i.e., an edge dislocation) at the attachment interface (Figure 1e). We also observe vacancies inside the lattice (Figure 1f) and point defects (extra NC in the lattice in Figure 1g). The dynamic process closely coupled to the NC interactions leads to the self-elimination of these defects (Movie S1).

2.2. Theoretical Calculations of Forces Acting on the NCs in the Superlattice. To understand the transient nature of the particles/clusters, we developed continuum-based theoretical models to calculate the interaction forces (F) and torques (τ) among NCs, including F_{vdW}/τ_{vdW}, F_{Sh}/τ_{Sh}, and F_{Br}/τ_{Br}, based on the NC positions obtained from detailed TEM image analyses. Based on the previous report, a volume element-based model in which a collection of infinitesimal cubical volume elements represent the particle, is used to calculate F_{vdW}/τ_{vdW} between two NCs at arbitrary configurations (see details in SI-1.1, 1.2, Figures S1−S4 and Table S1).[39] This model is based on the Hamaker's approach complemented by the Lifshitz theory:

https://doi.org/10.1021/acsnano.3c08610
ACS Nano 2024, 18, 32386−32400

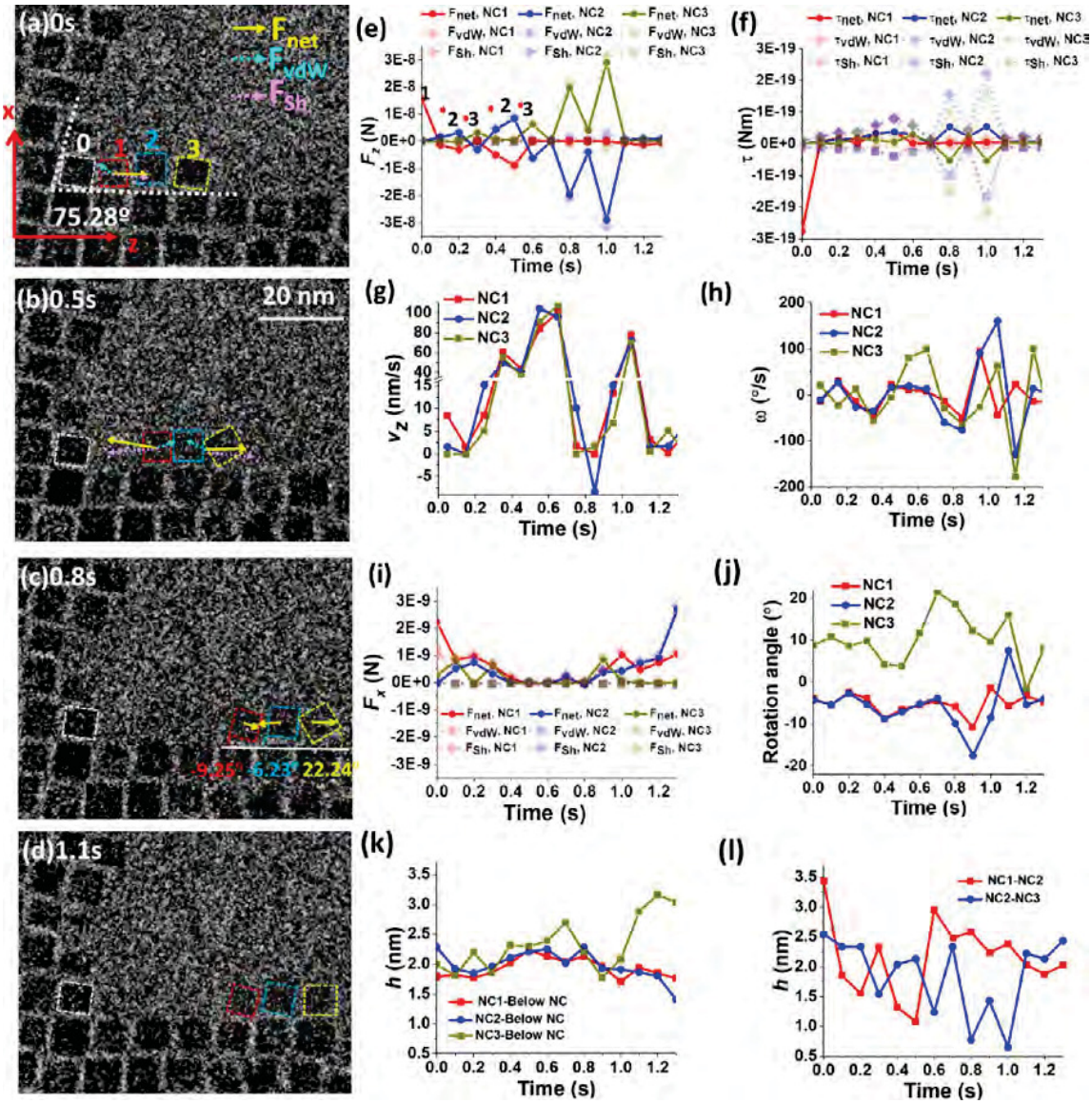

Figure 3. Calculated forces, torques, and measurements of the rotation angle and the translational and rotational velocities of outer NCs on a flat peripheral boundary. (a−d) Snapshots from the in situ TEM movie, showing the migration of clusters NC 1, NC 2, and NC 3. (e) Force and (f) torque acting on NCs 1, 2, and 3 along the *z*-direction, (g) translational velocity along the *z*-direction, (h) angular velocity (ω), and (j) rotation angle (θ) of NC 1, NC 2, and NC 3 as a function of time: (i) *x*-directional F_{vdW}, F_{Sh}, and F_{net} of NC 1, NC 2, and NC3, and (d) *z*-directional F_{vdW}, F_{Sh}, and F_{net} of NC1, NC2, and NC3. (l) Separation distance h of NC 1−NC 2 and NC 2−NC 3, with (k) h of NC1−NC below, NC2−NC below, and NC3−NC below. The *x* and *z* directions are described in (a) as red arrows. The *z*-direction is defined as θ = 0°.

$$U_{vdW} = -\left(\frac{A}{\pi^2}\right)U_R \quad (1)$$

where U_{vdW} represents the van der Waals interaction energy and A denotes the Hamaker constant. The Hamaker constant was computed using frequency-dependent dielectric responses of Pd and toluene, based on the Lifshitz theory, and its value was determined to be 2.61×10^{-19} J. Here, U_R represents the geometric parameters, which were estimated through numerical schemes based on slices of the NC building blocks (see eqs S15,16 and SI-1.2). F_{vdW} and τ_{vdW} are calculated by numerically differentiating U_{vdW} with respect to h and the rotational angle (θ), respectively. Note that the formulation does not include all of the complexities in the experimental system associated with the Si_xN_y membrane, thereby underestimating F_{vdW}. The details and additional factors influencing particle interaction analyses are discussed in Section 2.7.

Ligand interactions (F_{Lg}) include a repulsive steric hindrance force (F_{Sh}) when ligands overlap and an attractive force when ligands are separated. We first developed a method to calculate F_{Sh} and τ_{Sh} for anisotropic cubic NPs via the modified de Gennes models (see details in SI-1.1,1.3, Figures S1,S2, S5−S7 and Table S2).[40] The attractive nature of ligands does not result from the continuum description and will be discussed later alongside MD (Section 2.5). Based on de Gennes's continuum model, F_{Sh} is described as:

https://doi.org/10.1021/acsnano.3c08610
ACS Nano 2024, 18, 32386−32400

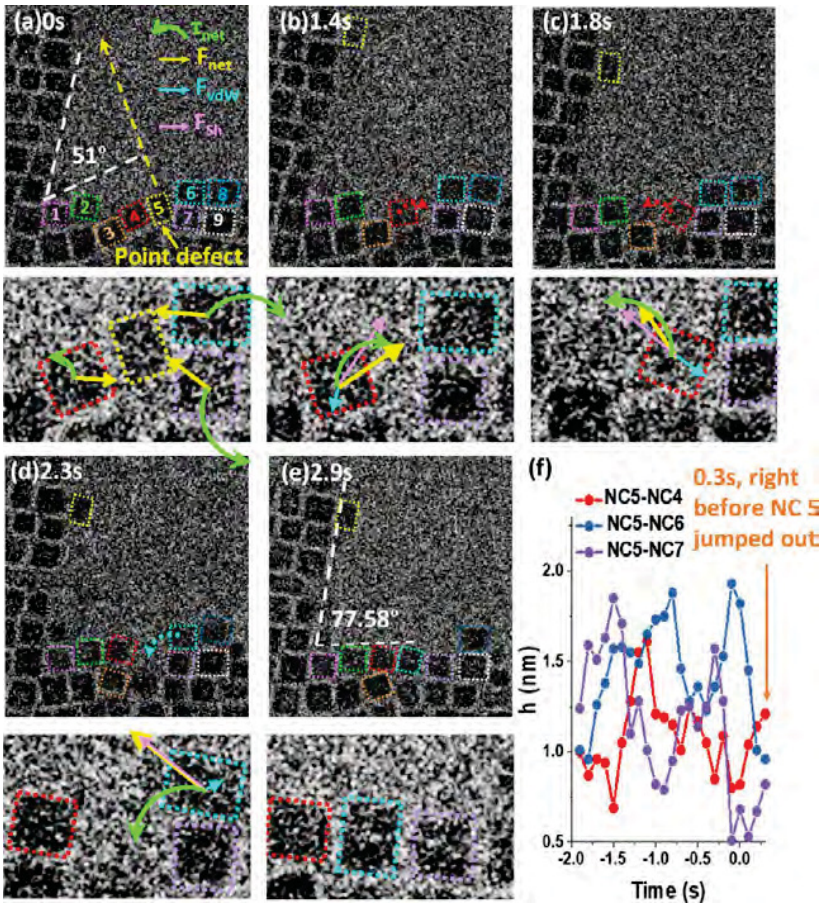

Figure 4. Self-elimination of a point defect. (a−e) Snapshots of an *in situ* TEM movie demonstrating self-elimination of the vacancy defect. The length of the arrows indicates the logarithm scale of the calculated magnitude of F_{net}, F_{vdW}, F_{Sh}, and τ_{net}. (f) Measured h of NCs 5−4, NCs 5−6, and NCs 5−7 before NC 5 jumped out. Dashed arrows indicate the moving direction of the NCs with magnitudes scaled logarithmically.

$$F_{Sh} = \tilde{A}\frac{kT}{s^3}\left[\left(\frac{2L_g}{h}\right)^{9/4} - \left(\frac{h}{2L_g}\right)^{3/4}\right](2L_g \le h),$$

$$F_{Sh} = 0(2L_g > h) \quad (2)$$

where k is the Boltzmann constant, h is the distance between particles, T is the system temperature, L_g is the ligand length in toluene, s is the mean distance between ligand attachment points, and $\tilde{A}$ is the area of overlapping ligands. According to the configuration, we obtained a net directional force (F_{net}) and torque (τ_{net}) from the vector summation of relevant forces and torques, respectively (details in SI-1.4). F_{Br} can be calculated by the fluctuation−dissipation theorem for a cubic particle (see details in SI-1.5 and Figure S8):

$$\langle F_{Br}(t)F_{Br}(0)\rangle = 8\pi k_B T\mu L\mathcal{K}_{t,ij}\delta(t) \quad (3)$$

$$\langle \tau_{Br}(t)\tau_{Br}(0)\rangle = 5\pi k_B T\mu L^3\mathcal{K}_{r,ij}\delta(t) \quad (4)$$

where $1/\mathcal{K}_{t,ij}$ and $1/\mathcal{K}_{r,ij}$ are the translational and rotational mobilities for an isolated cube, respectively, μ (0.56 mPa·s) is the viscosity of toluene, L is the cube size, and $\delta(t)$ is a delta function in time.

We first calculate F_{vdW} and F_{Sh} between a pair of face-to-face NCs (Figure 2a inset). The equilibrium separation (h_{eq}) of ∼2.25 nm, where F_{Sh} is balanced by F_{vdW}, is of the same order as that of the experimental average h (1.6−1.8 nm). A difference between h_{eq} and the experimental average h is expected due to the complexity of experimental conditions that are not considered in the calculations (see Section 2.7 for details), such as the presence of the Si_xN_y membrane, the unequal NC sizes (Figure 1a,b), and attraction between ligands when cubes are separated. In the experiments, the cubes are not in perfect parallel face-to-face configurations but exhibit a range of misalignments (Movie S1 and Figures 1−9). The defects in the superlattice and nonuniformity of particle sizes (∼5−12 nm) introduce dynamic disorder. In addition, we predict a sharp decay over a distance of ∼2 to 2.25 nm for F_{Sh}; i.e., F_{Sh} drops from $\sim 2 \times 10^{-9}$ N to zero within 0.25 nm (Figure 2a). This sharp decrease of F_{Sh} to zero, in contrast to a slow decrease in F_{vdW} to $\sim 5 \times 10^{-11}$ N, introduces "locally" imbalanced forces among NCs during particle motions. Based on the NC positions, orientations, and sizes obtained from *in situ* LP-TEM images and using the above expressions for the forces, we calculated F_{vdW}/τ_{vdW}, F_{Sh}/τ_{Sh}, and F_{Br}/τ_{Br} as a function of time (Figure 2b,c). On average, F_{Sh}/τ_{Sh} is larger than F_{Br}/τ_{Br}, while F_{vdW} and τ_{vdw} are the smallest force and torque, respectively. The majority of F_{Sh} values range from $\sim 10^{-10}$ to 10^{-8} N and are ∼1−2 orders of magnitude larger than F_{vdW} (10^{-11}−10^{-10} N). The imbalance between vdW and steric hindrance forces/torques is localized at different locations and different times across the superlattice, inducing

https://doi.org/10.1021/acsnano.3c08610
ACS Nano 2024, 18, 32386−32400

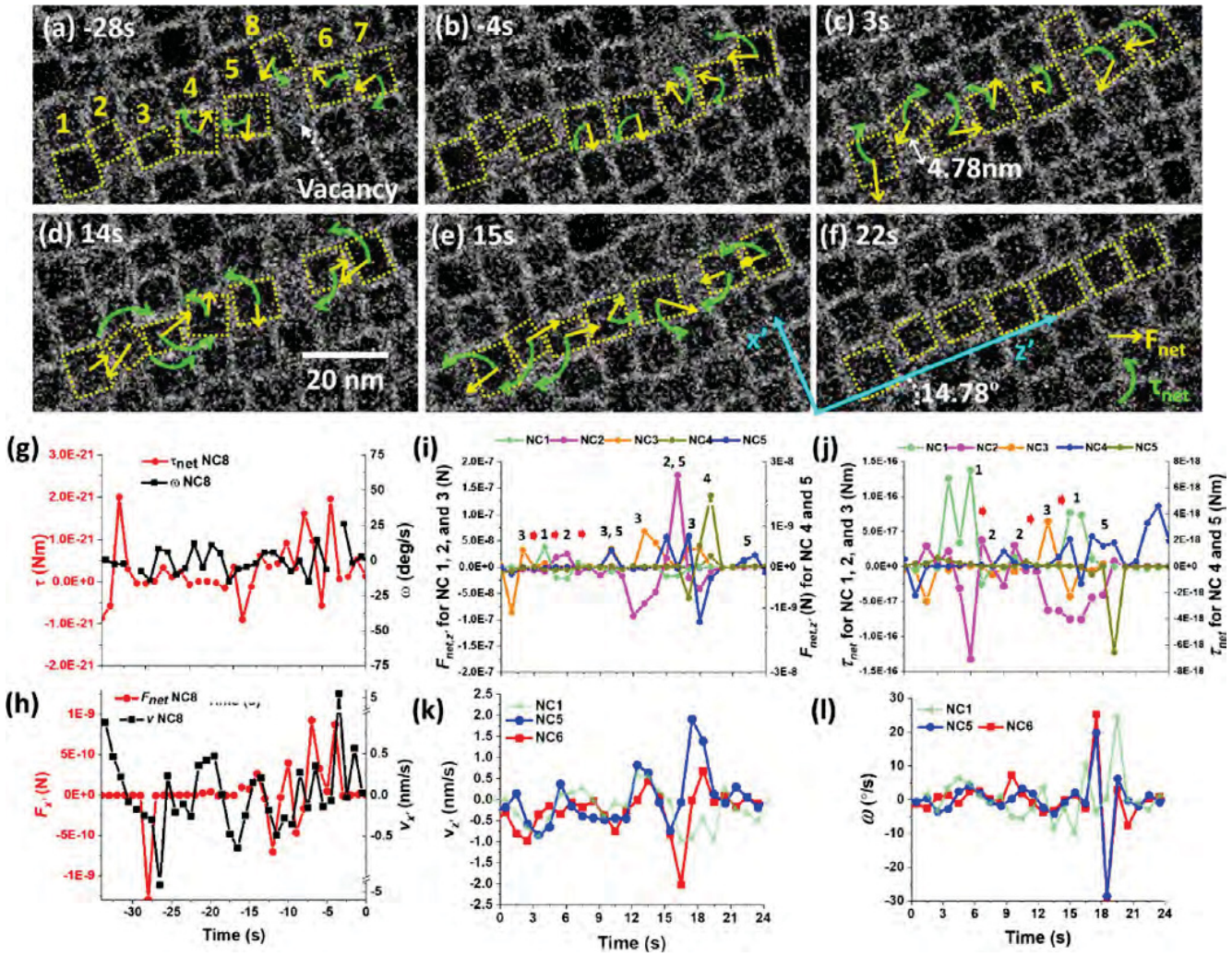

Figure 5. Self-elimination of a vacancy. (a−f) Snapshots of an in situ TEM movie showing self-elimination of the point defect. The length of arrows indicates the logarithm scale of the F_{net} and τ_{net} magnitudes. (g) τ_{net} and ω of NC 8 as a function of time, (h) $F_{net,x'}$ and $v_{x'}$ of NC 8 as a function of time, and (i, k) $F_{net,z'}$ and $v_{z'}$ of NCs as a function of time, respectively. (j, l) τ_{net} and ω of NCs as a function of time.

the dynamics of the superlattice and defect self-elimination, while the NCs in the superlattice remain assembled. F_{Sh} and F_{vdW} are in a similar range of 10^{-12} to 10^{-7} N (Figure 2c), driving and maintaining the assembled clusters at near-equilibrium with defects. Therefore, localized perturbations driven by the stronger steric forces and torques should be responsible for inaugurating such rich dynamics within the superlattice. These localized, unbalanced forces across the assembled structure are consistent with our observations of the dynamic aspects of the superlattice, such as constant NC motions of rotation and migration and of defect healing. Furthermore, the modified de Gennes models do not consider the attractive interactions among ligands (h is slightly >2 L_g), which contributes to holding NCs together. This will be discussed further in a later section on MD simulations (Section 2.5). F_{Br} (~10^{-10} N) resulting from thermal energy introduces additional disorder but lies within the range of F_{Sh} and F_{vdW}, and its mean value is slightly smaller and larger than the peaks in the distributions of F_{Sh} and F_{vdW}, respectively. The cubical shape induces τ_{Sh}, τ_{vdw}, and τ_{Br} ranging from 10^{-23} to 10^{-17} Nm. In contrast to the forces, τ_{Sh} is significantly larger than both τ_{vdw} and τ_{Br}, further demonstrating the dominant role of steric hindrance, especially in terms of the torque and the resulting rotational motions induced by ligand interactions.

We find that the direction of F_{vdW} aligns primarily with the lattice lines (Figure S9a) toward the neighboring NCs in the square superlattice, shown as the tetra-modal distribution of angles at ~ −110°, ~ −20°, ~70°, and ~160° (Figure S9b), and is primarily determined by the neighboring NCs due to the large size (~7.5 nm) of the NCs, i.e., the effective attractive F_{vdW} (see details in Figure S9). This tetra-modal distribution is different from our previous study of ~3 nm Au-NP self-assembly, in which F_{vdW} points to the center of the cluster.[11] F_{Sh} and F_{net} have a similar tetra-modal distribution (Figure S9c−f). As a general trend, the direction of F_{Sh} is typically opposite that of F_{vdW}. F_{Sh} has a more pronounced tetra-modal distribution due to its stronger dependence on separation than F_{vdW}, leading to a clear tetra-modal distribution for F_{net}. To obtain a mechanistic understanding of the roles of F_{vdW} and F_{Sh} for complicated cases, we consider three simple but representative benchmark cases (Figure 2d−k) that can correlate to translational and rotational behaviors of NCs in the experiments (Figures 3 − 6).

Case 1: The translational motion of an NC between two lines of perfectly aligned NCs (Figure 2d). F_{vdW_z} oscillates

https://doi.org/10.1021/acsnano.3c08610
ACS Nano 2024, 18, 32386−32400

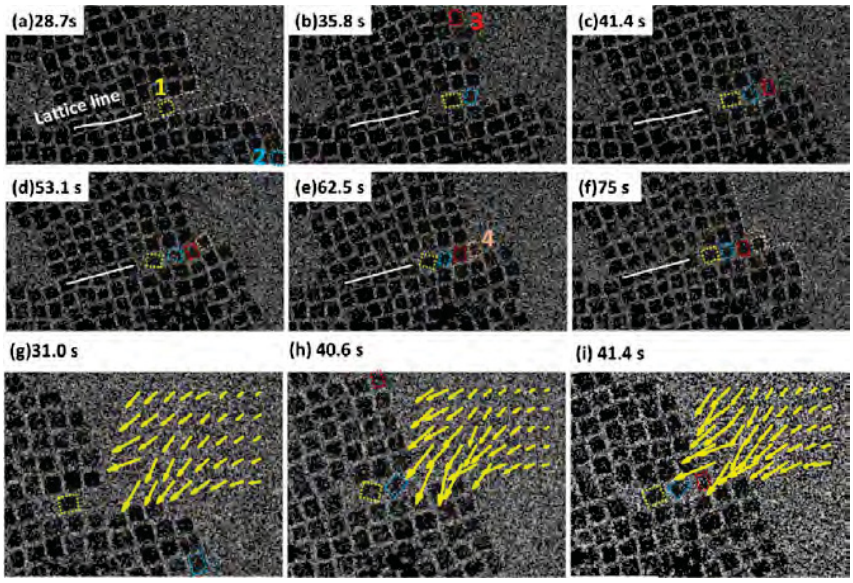

Figure 6. Peripheral boundary smoothness. (a–f) Snapshots of *in situ* TEM movie showing self-elimination of the line vacancy defect created by the attachment of the two clusters (Figure S15) at 0 s. (g–i) The vdW force fields near the line vacancy defect at 31.0 (g), 40.6 (h), and 41.4 s (i) before NCs 2, 3, and 4 enter the line vacant space, respectively. The positions of the vdW force field arrows changed because the superlattice migrated to the upper portion of the viewing area as a function of time (Movie S1).

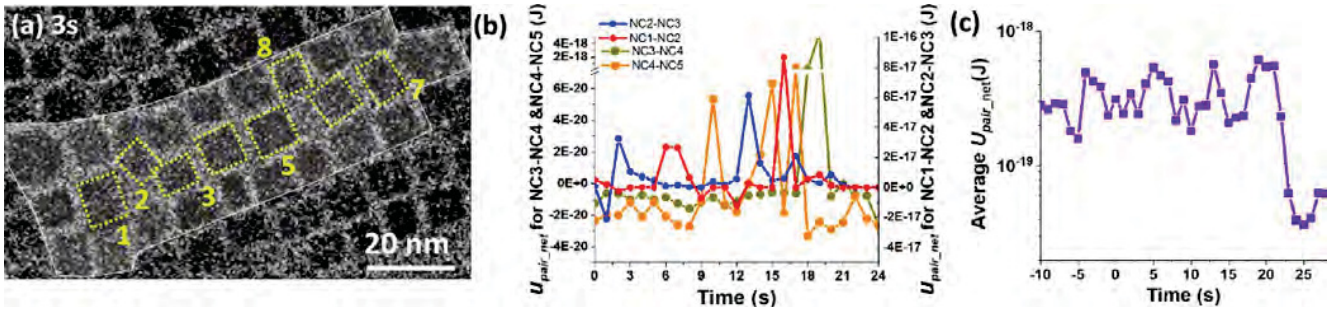

Figure 7. (a) TEM image showing the NCs that are counted for the average U_{pair_net}. (b) U_{pair_net} for NC 3–NC 4 and NC 4–NC 5 as a function of time. (c) The average U_{pair_net} (U_{pair_vdW} + U_{pair_Sh}) of the NCs outlined by the white area as a function of time.

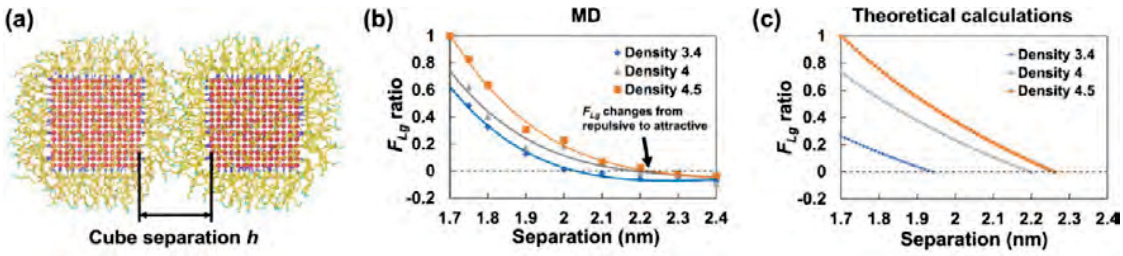

Figure 8. MD simulations of the ligand interaction force. (a) Atomic model of the face-to-face configuration of Pd NCs in MD simulations. (b,c) The ligand interaction as a function of h from MD simulations and theoretical calculations, respectively, plotted as ratios.

periodically with an amplitude of 2×10^{-11} N (Figure 2e). Due to the perfect alignment, F_{Sh_z}, F_{net_x}, and $\tau_{\_net}$ are zero. The periodic change of the relative positions of the neighboring top and bottom NCs leads to oscillation of the F_{net_z} direction, demonstrating that an additional driving force is required for the NC to move from a state of repose ($F_{net} = 0$). Similarly, a driving force is needed for NPs to move toward the most energetically stable state, because the oscillating F_{net} acts as a set of barriers.

Case 2: The translational motion of an NC along with the disordered (two tilted NCs) bottom line (Figure 2f). When the moving NC encounters the tilted NC, both F_{Sh_z} and F_{Sh_x} increase significantly up to the order of 10^{-9} N due to the reduced h, becoming the dominant forces and increasing the magnitude of force oscillation (Figure 2g). Unlike Case 1, the translational motion induces a torque, τ_{Sh}, that is on the order of $\sim 10^{-17}$ Nm based on the NC interactions (Figure 2h). Similarly, when we introduce variations in size, shape, and vacancy defects (Figure S10), these alterations lead to additional forces along the x-direction, torque generation, and a disruption in the perfect periodic oscillation of forces along the z-direction.

https://doi.org/10.1021/acsnano.3c08610
ACS Nano 2024, 18, 32386–32400

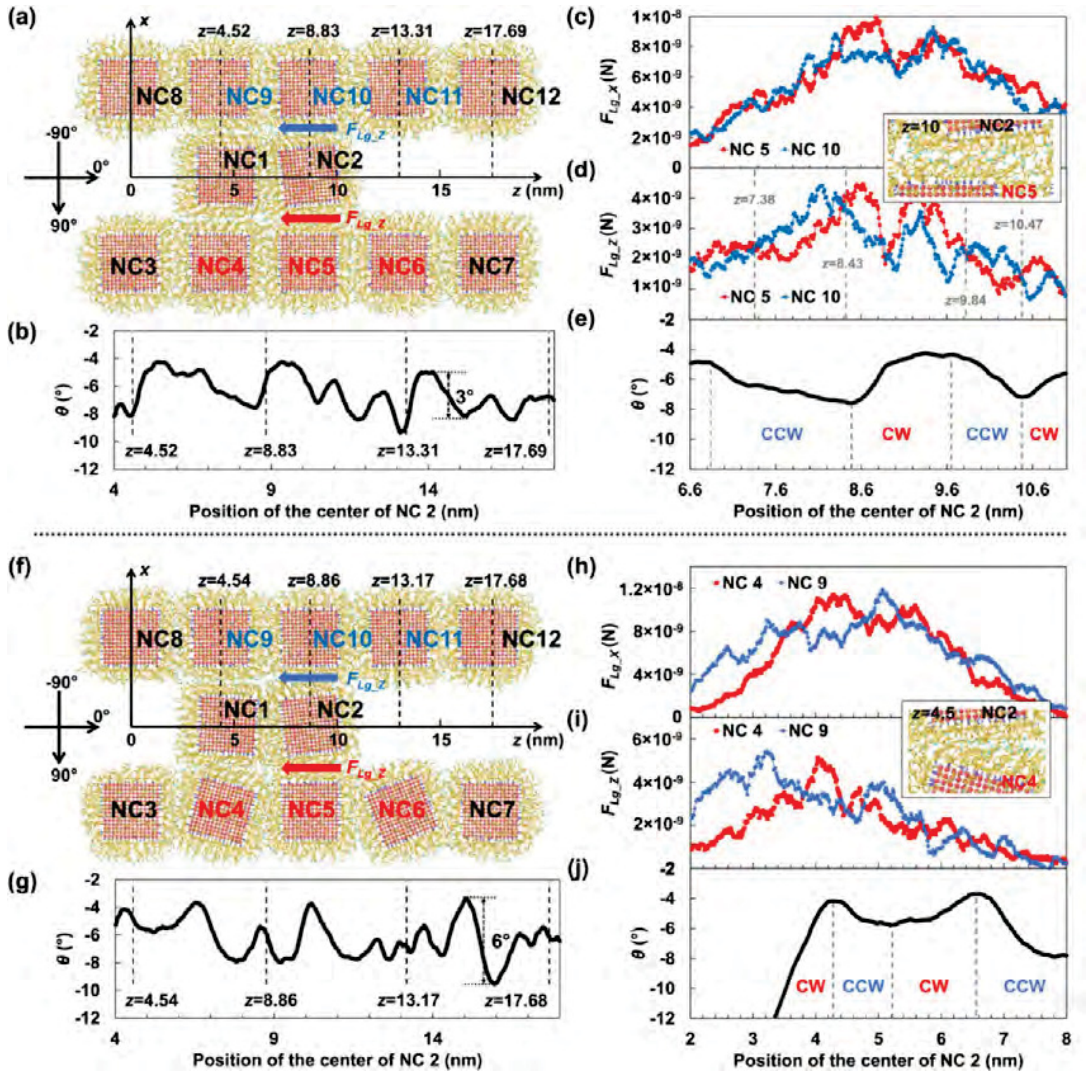

Figure 9. Two cases of MD simulations with 12 NCs. (a, f) The atomic model and definitions of the coordinates for positions and rotation angles. The position of (z = 0, x = 0) is defined as where NC 2 forms face-to-face configurations with NCs 3 and 8 and in the middle of them. The positions of other face-to-face configurations are marked by dashed lines. (b, g) The rotation angle θ of NC 2 as a function of its position. Three regions are marked by the four face-to-face positions as their boundaries (dashed lines). (c, d) The ligand interactions F_{Lg} on NC 2 from the wall NCs when it passes through NCs 5 and 10 (from z = 6.6 to 11 nm) in Case 1. The interactions along z (F_{Lg_Z}) are dragging forces. Consequently, the ligands on NC 2 lean backward, as is shown in the inset when NC 2 is at z = 10 nm. Positions are marked where F_{Lg_Z} from the top and bottom cross each other, indicating changes in the direction of the torque and subsequently the rotation. (e) θ of NC 2 during the same process with (c) and (d). The rotation (marked by CW [clockwise] and counterclockwise [CCW]) is generally consistent with the torque caused by the F_{Lg_Z}. (h) The ligand force along the x-direction (F_{Lg_X}) from the wall NCs on NC 2 from z = 2 to 8 nm in Case 2. (i, j) Draging F_{Lg_Z} on NC 2 from the wall NCs and θ during the same process as (h).

Case 3: The rotational motion of an NC above two other NCs (Figure 2i). In this case, F_{net_x}, F_{net_z}, and τ_{net} are induced and the total force is dominated by F_{Sh} (Figure 2j,k). Clockwise (CW) rotation of the NC from the 0° position induces a positive F_{net_x}, negative F_{net_Z}, and negative τ_{net} (direction of CW) due to the decreased h between the top NC and the bottom-left NC. At a 45° rotation angle, due to the perfect reflection symmetry, F_{net_z} and τ_{net} are zero. The oscillations of F_{net_z} and τ_{net} indicate that an additional driving force is needed for an NC to move from left to right, as shown in Figure 2.

Overall, the benchmark calculations indicate that F_{net} and τ_{net} oscillate, corresponding to the NC motions, and the periodicity and magnitude of the oscillations directly result from the NC interactions. The F_{Sh}/τ_{Sh} generated by imperfect superlattice structures dominate over F_{vdW}/F_{Br} and τ_{vdw}/τ_{Br}, respectively, triggering NC movements in the defective region. Similar results were obtained for several different geometrical arrangements (Figure S10). Based on our benchmark case calculations (Figure 2), F_{net} and τ_{net} are dominated by F_{Sh} and τ_{Sh}, respectively, in the transient superlattice. In the following discussion, we only presented F_{net} and τ_{net} for simplicity.

2.3. Case Studies on NC Motion and Defect Self-Elimination Processes. For the practical experimental configurations, the NCs are not perfectly aligned due to the variations in cube size and shape as well as defects. Therefore, the NC motions are frequently disturbed due to the unbalanced forces between F_{vdW} and F_{Sh} at the defective regions, as well as Brownian forces. Over time, the defects are

https://doi.org/10.1021/acsnano.3c08610
ACS Nano 2024, 18, 32386−32400

self-eliminated. Here, we categorize several canonical NC motion behaviors and the resulting defect self-elimination.

2.3.1. NC Migration on the Peripheral Boundary of the Superlattice Cluster. Three NCs-1, 2, and 3 migrate from left to right as a whole (Figure 3a–d). At the kink site of the experimental superlattice, the vertical lattice line is tilted at an angle of 75.28°, with respect to the 90° angle of a perfect superlattice (Figure 3a). This leads to a small h of 0.75 nm between NC 0 and NC 1, and thus a calculated repulsive F_{Sh} along the z-direction (F_{Sh_Z}, 1.56×10^{-8} N) that is stronger than the attractive F_{vdW_Z} (-2.91×10^{-10} N). This repulsive F_{Sh} triggers the translational motion of NC 1 to the right (0 s, Figure 3e). Consequently, the h between NC 1 and NC 2 decreases due to a "chain interaction" by transmitting the driving force from NC 1 to NC 2 and from NC 2 to NC 3, as transmitted from NC 0 to NC 1 (0–0.6 s, Figure 3e). The chain interactions are manifested by the oscillation of $F_{net\text{-}z}$ and τ_{net}, e.g., (1) the oscillation of the force magnitude on each NC (Figure 3e) and (2) the alternating decrease and increase of $F_{net\text{-}z}$ among the three NCs. For example, from 0 to 0.2 s, NC 1 has a decreased $F_{net\text{-}z}$ while NC 2 has an increased $F_{net\text{-}z}$. From 0 to 0.5 s, the largest positive $F_{net\text{-}z}$ is on NCs 1, 2, and 3 at 0, 0.2, and 0.3 s, respectively. τ_{Sh} follows a similar oscillation pattern (Figure 3f). While NCs 1–3 move translationally on the flat peripheral boundary at a velocity (v) of ~36 nm/s on average (up to ~100 nm/s, Figure 3g), they also rotate within an angle (θ) of ~±20° and angular velocities (ω) of up to ~±170°/s (Figure 3h). All v, θ, and ω are measured based on NC positions as a function of time obtained from *in situ* TEM movies. The average oscillation frequency (f) of $F_{net\text{-}z}$, τ_{net}, v, and ω is similar and on the order of ~2.5 s^{-1}. In conclusion, the trigger force induced by F_{Sh} at the defect region initiates the chain interactions in particle movements.

To understand the subsequent interactions between NCs and the NCs below them, as well as their resulting motions, we calculate the force and measured the h between NCs 1, 2, and 3 and the NCs below them (Figure 3i,k). The values of h mostly range from 1.5 to 3.5 nm and are slightly larger than that (0.5 to 3 nm) between NC 1 and NC 2, and between NC 2 and NC 3 (Figure 3l). When F_{net_x} is close to zero, h ranges from 2 to 2.5, which is close to the h_e (~0.4–0.8 s in Figure 3i, k). The decreased F_{net_x} leads to a significant increase in particle mobility (e.g., increased v_z). Note that although F_{net_x} is 1 order of magnitude smaller than F_{net_z}, it is sufficient to affect the motions of NCs along the z-direction.

On a nonflat peripheral boundary that results from the stepwise assembled NC superlattice, the NC often encounters obstacles during migration along the peripheral boundary and vigorous rotational movements (see details in Figure S11).

2.3.2. Point and Vacancy Defects in the Superlattice. The point defect with an extra NC in the lattice structures is self-healed through highly enhanced compression, which induces a strong F_{Sh} acting as a trigger force. Due to the extra NC 5 in the lattice line, the angle between two lattice lines (white lines in Figure 4a) at the kink site is 51° at the 0 s, reducing h between NC 5 and its neighboring NCs (0.5–1.8 nm) and causing compression among them. The small h of 0.5–1 nm induces a momentary and significantly high F_{Sh}, and thus a F_{net} from NCs 4, 6, and 7 toward NC 5 (Figure 4a bottom), pushing NC 5 off the cluster (Figure 4a,b). Afterward, NC 4 has strong F_{Sh} and τ_{Sh} toward the vacancy created by the departure of NC5 (Figure 4b bottom), thus moving to the vacancy and making contact with NC 7 at a high v (v_z = 35.575 nm/s and v_x = −4.48 nm/s) and ω (−150.99°/s) (Figure 4b,c S13), leading to a small h between NCs 4 and 7 at 1.8 s. Subsequently, through chain interactions, NCs 1–7 are roughly aligned, relaxing the angle between two lattice lines at the kink site from 51° to 77.58° (Figure 4e). The bottom panels of Figure 4a–d demonstrate that the NC motions follow the calculated F_{net}, indicating that the calculation method is reasonable for this work and confirming the dominant role of ligands. The NCs consistently show their characteristic oscillations of force, torque, translational velocities, and angular velocities during the whole process (Figure S13). The oscillation frequency (f) of h is ~0.67 to 1 s^{-1} from −2 to 0 s before NC 5 jumps out of the lattice (Figure 4f).

The vacancy introduces unbalanced F_{Sh} to its neighboring NCs, resulting in NCs moving toward the empty space and the vacancy migrating through dynamic NC motions (Figure 5a–c). Eventually the vacancy is self-eliminated (Figure 5d–f). Vacancy defects typically generate tensile strain due to extra free space in the lattice. However, due to the dynamics of the superlattice, compressive strains in our study are often observed temporarily and locally (Figure 5a–e). At 3 s (Figure 5c), the highly compressive strain between NCs 2 and 3 induces strong repulsive forces and torques that are transmitted to NC 5 through chain interactions. The magnitudes and directions of F_{net} and τ_{net} oscillate and alternate among NCs 1–5 (Figure 5i,j), similar to the peripheral boundary NC migration in Figure 3. We note that the chain interactions are not perfectly sequential from NC 1 to NC 5 (Figure 5i,j) due to the interactions with additional surrounding NCs other than NCs 1–5. The chain interactions are not in 1D but are in a 2D network, eventually leading to NCs 1–5 moving toward the vacancy (Figure 5d–f).

Due to the slow motion of the NCs inside the superlattice, we are able to capture the corresponding characteristic oscillation (both magnitude and direction) of v and ω and their alternation among NCs during the chain interactions, showing NCs 1, 5, and 6 as examples (Figure 5k,l). The average oscillation frequency f of the chain interaction of $F_{net\text{-}z}$ is ~0.33 s^{-1}, which is on the same order as the f of both v (~0.22 s^{-1}) and ω (~0.32 s^{-1}). This is significantly slower than the f of the outer NC motions (2.5 s^{-1}) (Figure 3e–h). Through the oscillated chain interactions, NCs fill the vacancy (Figure 5e,f).

The motions (represented by v and ω) of the NCs in the peripheral boundary are faster than those within the cluster (~10^1 nm/s and ~5×10^1 °/s vs ~10°nm/s and ~10^1 °/s) due to more free space vs limited space, respectively (Figure 3g,h and Figure 5k,l). Correspondingly, it takes longer to self-eliminate a vacancy defect inside of the superlattice (~22 s, Figure 5) than a point defect in the peripheral boundary (~1.4 s, Figure 4).

2.3.3. Edge Dislocations in the Superlattice. We find that the attachment of two clusters induces a defect at the attaching peripheral boundary and that the defect has an extra half-line of NCs in the 2D superlattice (Figure S15a,b). This extra half-line is introduced by the step-edge boundary of one cluster (white dashed line in Figure S15a). We define the defect as an edge dislocation at the nanometer scale, and it is self-eliminated after ~30 s via the chain interactions of the unbalanced forces and torques exerted on the NCs at the edge-dislocation region (details in Figure S15a–f, S16). These behaviors are analogous to atoms but, instead, originate from

https://doi.org/10.1021/acsnano.3c08610
ACS Nano 2024, 18, 32386–32400

their nanoscale dimensions.[41] NPs could be described as "artificial atoms." At the atomic scale, the OA of two NPs with a slight misalignment form a defect, called edge dislocation, where an extra half-plane of atoms is introduced midway through the crystal lattice and the edge dislocation is self-eliminated within a few seconds.[42]

2.3.4. Flattening of the Peripheral Boundary. Besides edge dislocation, a vacancy or a line of vacant space (line vacancy) can also form at the attaching surface after attachment of the two clusters, resulting in an uneven peripheral boundary (Figure 6a). When the peripheral NCs reach the region near the line vacancy, the direction of F_{vdW} is toward the line vacancy (Figure 6g–i) and attracts NCs to the vacancy, enabling the collective assembly of NCs. Here, F_{vdW} dominates and typically points toward the cluster's center of mass, whereas F_{Sh} is negligible due to no overlap of ligands in the free space. Although F_{Br} ($0–1.00 \times 10^{-10}$ N) is 1–4 orders of magnitude larger than F_{vdW} ($10^{-10}–10^{-15}$ N), statistically F_{Br} can be disregarded due to its random nature in both magnitude and direction. Afterward, NCs move slowly within the line vacancy due to the confinement, with f (~0.2 s^{-1}) of the oscillation of translational and rotational velocities similar to that of the inner NCs that fill one vacancy (Figure 5).

We notice that NCs move very fast on the peripheral boundary (Figure 3g and Movie S1) and can easily reach the line vacancy from far away (i.e., no need for the neighboring NCs to fill the vacant space). They either pass by the vacant space or are stopped by the stepped peripheral boundary and fill the vacant line (Figure 6a–f). We noticed that the NCs can jump over a few NCs or a very long distance to the line vacancy. NCs 2 and 3 jump over NCs 2 and 4 and reach the vacancy (Figure 6 and Movie S1). NC 4 moves too fast to be tracked to its original location, but NC 4 has possibly traveled across half or one of the superlattices because no nearby NCs were seen filling the vacancy.

Our study of defect self-elimination mechanisms across different defect types reveals that these defects can be alleviated through successive translational and rotational motions initiated by a driving force. This force, inadvertently produced by the unbalanced forces and torques in defective regions or by a momentarily reduced value of h due to Brownian motion (Figures 3–6 and S11–S17), propagates through the chain of interactions at specific frequencies, leading to defect self-elimination. Specifically, point defects and edge dislocations induce compressive strain at the defective regions, while vacancy defects result in tensile strains. The driving forces for point defects, vacancy defects, and edge dislocations are associated with interactions caused by ligand-induced steric hindrance among the NCs. On the other hand, the smoothness of the peripheral boundary is governed by van der Waals attractive forces, which can pull the moving NCs along the boundary near the defective regions.

2.4. Evolution of Pair Potential and Shape Effect on Three-Body Configurations. *2.4.1. Evolution of Pair Potential During Defect Formation and Elimination Processes.* As noted, the defects introduce imbalances in forces and torques among the NCs and instability of the system. To correlate the imbalance to variations in the potential energy during defect formation and elimination processes, we calculated the "average" pair potential (U_{pair}) over the areas where the defects were formed and eliminated:

$$U_{pair} = \frac{\sum U_{i-j}}{\text{the number of pairs}} \quad (5)$$

where U_{i-j} indicates the relevant pairwise interaction potential (i.e., van der Waals interactions (U_{vdW}) and steric hindrance interactions (U_{Sh})) between NC_i and NC_j, in which i and j indicate the NC index.

The assembled structures exhibited energetic instabilities due to defects in the system. One representative example is elimination of a vacancy inside the superlattice (Figure 5). We see the momentary increase of the individual $U_{\_NC1\text{-}NC2}$, $U_{\_NC2\text{-}NC3}$, $U_{\_NC3\text{-}NC4}$, and $U_{\_NC4\text{-}NC5}$, and these alternate with time due to the chain of interactions (Figure 7a,b), resulting, on average, in stepwise energy barriers (Figure 7c). After the vacancy is eliminated, U_{pair_net} significantly decreases by about 1 order of magnitude. Other examples show that the assembled structures exhibit energetic instabilities (increasing) as defects emerge and are eliminated (Figures S18 and S19).

2.4.2. Shape Effect on Three-Body Configurations. The calculated pair potentials (Figure S20) show that for cubes the face-to-face configuration is the most stable, consistent with our observation that one NC tends to stay on top of another NC (face-to-face configuration) instead of between two NCs (brick-wall configuration). Thus, we can capture only clear images of face-to-face configurations while NCs migrate along a flat peripheral boundary at a velocity of up to 100 nm/s (Figure 3a–d). The energy barrier for NCs to pass another NC is $\sim 1 \times 10^{-19}$ J (Figure S20c). In contrast, for spheres, the triangular configuration (comparable to the brick-wall configuration) is the most energetically stable rather than the L-configuration (comparable to the face-to-face configuration), indicating that the shape of particles plays a critical role in the resulting pattern of particle assembly.

2.5. Classical MD Simulations. To gain more complementary insight into the ligand interactions and NC behaviors from an atomistic perspective, MD simulations of ligand-coated Pd NCs are conducted using the LAMMPS package based on the explicit-atom model (see SI-3 for detailed information), which allows us to consider and investigate the effect of attractive ligand interactions in addition to the repulsive steric hindrance interactions.[21,43] A comparison of F_{Lg} (normalized ratio) from MD and F_{Sh} from theory for a pair of parallel NCs (Figure 8a) shows consistent trends in slope and crossover from repulsive to attractive, where F_{Lg} increases with increasing ligand density and decreasing h, and the crossover point moves to larger h with increasing ligand density (Figure 8b,c). In addition, MD predictions reveal a stronger dependence of F_{Lg} on h for $h < \sim 2$ nm. Therefore, we expect that MD simulations can capture the steric hindrance interactions to a reasonably correct extent, while the magnitudes of forces may deviate from continuum-based theory (Figure S25). The equilibrium length of coated ligands for a single cube is ~1.13 nm extending from the Pd (100) surface with a ligand density of 4.5/nm^2, which is close to the experimental value of 4.2/nm^2 (see SI-3). For this density, F_{Lg} is repulsive when $h < 2.25$ nm—approximately two times the length of coated ligands on a free-standing NC—and becomes attractive when h is larger than 2.25 nm (Figure 8b).

Another advantage of MD is its ability to directly model and investigate dynamic processes of NC motions that cannot be captured by static theoretical calculations. Thus, we further conduct MD simulations to investigate the mechanism of NC motions from a molecular perspective. Owing to a possible

https://doi.org/10.1021/acsnano.3c08610
ACS Nano 2024, 18, 32386–32400

difference between the experiments and MD simulations to directly compare the dynamic nature of NCs, we first examine the consistency of translational (D_t) and rotational (D_r) diffusivities (see SI-3.1 for method detail). Our simulation predicts $D_t = 7.53{\cdot}10^{-11}$ m^2/s and $D_r = 1.18{\cdot}10^{7}$ rad^2/s, which are on the same orders as those predicted from the Stokes−Einstein relation ($D_t = 1.59{\cdot}10^{-10}$ m^2/s and $D_r = 1.90{\cdot}10^{7}$ rad^2/s), respectively. Therefore, although MD is not accurate for vdW interactions at long ranges (>1 nm), we expect that MD simulations can reasonably explain dynamic behaviors of Pd NCs that are dominantly triggered by F_{Lg} from ligands.

Simulations of two cases with 12 NCs are subsequently performed (see SI-3.1 for the method details). Here, we investigate the behavior of NC 2 because it is only driven by interactions with other surrounding NCs-only the motion of NC 2 from z = 4.52−17.69 nm for Case 1 (Figure 9a) and z = 4.54−17.68 nm for Case 2 (Figure 9f) are considered. In those regions, both NC 1 and NC 2 are entirely inside the channel. As NC 2 moves through the channels, we observe rotation of NC 2 consistent with experimental observation of rotation by inner NCs along with translational motion, but with a smaller oscillation amplitude ($\Delta\theta \sim 3-6°$ in Figure 9b and g vs $\Delta\theta \sim 5-10°$ occasionally up to 20° in Figure S14c).

For Case 1, three cycles are manifested in Figure 9b corresponding to the positions of NCs 9, 10, and 11. In each cycle, NC 2 rotates CW first and then counterclockwise (CCW). Each cycle of the simulated rotation corresponds to the passage of an NC, similar to the oscillation of F_{vdW} magnitude from theoretical calculations in Figure 2d. The force from the ligand along the x-direction (F_{Lg_x}) contributes little to the rotation of NC 2 because F_{Lg_x} from the top and bottom are almost identical (Figure 9c)—thus, this contribution is trivial. However, F_{Lg_z} from the top and bottom wall NCs consistently act as dragging forces (Figure 9c,d)—a feature that is captured only by MD but not by theoretical calculations (Figure 2). This is corroborated by the observation of the ligand conformation on NC 2 where all ligands lean backward (inset of Figure 9c,d). F_{Lg_z} creates torques on NC 2 due to unbalanced drag forces from the wall NCs, thus causing rotation. Here, we only show F_{Lg_z} from the wall NCs that NC 2 passes through because they are the closest and have dominant F_{Lg} (Figure S26). For example, when NC 2 passes through NCs 5 and 10 (z = 6.6−10.8 nm), F_{Lg_z} from wall NCs is mostly dominated by top-wise interactions between NCs 2 and 10 from z = 7.38 to 8.43 nm (colored in blue in Figure 9d), leading to CCW rotation (Figure 9e). From z = 8.43 to 9.84 nm, F_{Lg_z} from the bottom wall NC 5 (colored in red in Figure 9d) is larger than its top counterpart (blue), creating a τ_{net} that rotates NC 2 CW (Figure 9e). Because NC 2 is tilted ∼− 10° while entering the channel, the θ of NC 2 is negative throughout the channel. Deviations exist between the regions marked by F_{Lg_z} crossing and NC rotation. This is expected considering the inertia of the NC, but they are generally consistent.

In Case 2, the disorder introduced by the tilted NCs 4 and 6 leads to a slightly larger amplitude of θ at ∼4−6° (Figure 9g) compared with ∼3−4° in Case 1 (Figure 9b). In addition, F_{Lg_x} from the top and bottom becomes asymmetric (Figure 9h) and disrupts the three main cycles of rotation corresponding to the periodic wall NCs 4, 5, and 6 in Case 1 (Figure 9b), leading to a more disordered oscillation (Figure 9g). For example, when NC 2 passes through NCs 4 and 9 (from z = 3.83 to 4.8 nm), the tilted NC 4 results in a small h at the bottom of NC 2 (inset of Figure 9h,i) and consequently a larger F_{Lg_x} than its top-wise counterpart. This creates a τ_{net} that rotates NC 2 in addition to F_{Lg_z}—thus, more factors contribute to the rotation of NC 2, and there is no explicit correlation between F_{Lg_z} and θ as in Case 1.

MD simulations capture the attractive ligand interactions in addition to the steric hindrance forces. This reveals their effects on NC motions during a dynamic process of NC movements, while underestimating the vdW interactions between NCs. The simulations provide further insights that F_{Lg} consistently acts as a dragging (i.e., attractive) force to the NCs and is associated with the movements of the NCs, while the continuum-based theory only considers repulsive force from ligands. By integrating simulations and theory, we explained the NC behaviors observed experimentally.

Further simulations (see details in SI-3.2) with varying ligand lengths—including a nine-carbon chain (C9), C12, and C15, and densities of 3.4/nm^2 (D3.4), D4.2, and D4.5—reveal that the longer ligand length and higher density (C12/D4.5 and C15/D4.5) show three clear cycles of oscillation (Figure S28b,c) in the rotation angle θ of NC 2, corresponding to passage of three NCs below NC 2 (Figure 9a). This aligns with stronger interactions with the bottom NCs in cases of longer ligand length and higher density (Figure S28a), as also seen in Figure 9b. This feature becomes unclear with shorter ligand lengths and lower density (C9/D4.5 and C12/D3.4, Figure S28d,e). Such results are consistent with our conclusion that ligand interactions are the major driving force behind the NC rotation.

2.6. Analogy of Particle Motions in a Superlattice to Atomic Vibration in a Crystal Lattice. The NC superlattice is an assembly of particles governed by attractive vdW and repulsive/attractive ligand interactions. The NCs can be considered analogous to atoms in a crystal governed by interatomic forces. In the experiments, the collective NC vibration (oscillations of translational and rotational velocities) can be thought of as analogous to "lattice vibrations" in the crystal lattice. The oscillation of nanoparticles near their equilibrium positions due to interactions between adjacent nanoparticles can be approximated as harmonic oscillations in which $F = -kx$, where F is the force, k is the spring constant, and x is displacement of the particle from its equilibrium position. Accordingly, an analogous "lattice vibration" can be calculated by applying lattice dynamics calculations.[44] The analogous "phonon" ("lattice vibration") is related to the NC mass and frequency of the NC oscillations and is propagated via chain interactions in the superlattice. We expect that both stronger spring constants among the NCs and smaller NC sizes would lead to a higher frequency of vibration or "phonons" with higher frequency, as predicted by lattice dynamics. Based on our study, we find that ligand interactions dominate, and the longer ligand length and higher density can analogously lead to a stronger spring constant.

2.7. Limitations of the Interpretation Based on Formulated Forces and Torques. F_{Sh}/τ_{Sh} calculations from the continuum-based theory that are based on the de Gennes' model are only effective when h is smaller than $2L_g$ (ligand length) and while ignoring the attractive ligand interactions when two NCs are leaving each other ($h > 2L_g$).[45] The F_{Lg} calculated by our MD simulations clearly shows attractive interactions when h is slightly larger than $2L_g$. This indicates that the NCs exist as one cluster in a dynamic form.

https://doi.org/10.1021/acsnano.3c08610
ACS Nano 2024, 18, 32386−32400

In our LP-TEM experiments, NCs are close to the Si_3N_4 membrane surface. This can change F_{vdW} between NCs because the Si_3N_4 membrane is an additional object that can perturb the vdW interactions between NCs.[46] In general, such a perturbation due to a nearby interface is expected to result in a stronger vdW attraction between particles (see SI-1.6, 4). As a result, the existence of the Si_3N_4 membrane near NCs can potentially result in an overestimate of h_{eq}.

Hydrodynamic nature can provide a valuable perspective for interpreting our experimental and theoretical results. We observe that larger forces and torques typically correspond to faster translational and angular velocities (Figures 3−5). However, the mobility of NCs is also correlated to the environment, such as separations from or configurations with neighboring NCs. First, the hydrodynamic mobility depends on the size ratio between NCs, which is analogous to the spherical particle case.[47] This indicates that an unequal pair of NCs is more mobile in their relative motions and closer to each other compared to a pair of equally sized NCs, leading to a smaller experimental h than the calculated h_{eq}. Therefore, the unavoidable size difference in NCs can cause a difference between the experimental average h and h_{eq}. Second, the strong separation dependence of the hydrodynamic mobility suggests a wide range of NC velocities depending on the configurations around the NCs. The hydrodynamic mobility decreases 2 orders of magnitude, when the h is decreased from 4 to 0.8 nm, considering the face-to-face configuration between NCs. Consequently, such a drastic decrease in the hydrodynamic mobilities can account for $\vec{v}_r$ and $\vec{\omega}_r$ that are 1−2 orders of magnitude lower at the movements in the step vacancy defect or inside the superlattice compared to surface migration or movements in an open space (i.e., no neighbors). For example, the oscillatory behavior of outer NCs is more pronounced than that of inner NCs because the additional free space can increase h, leading to an increase in hydrodynamic mobility (Figure 3). This increase is associated with higher translational and angular velocities (e.g., Figure S11). Details of the effects of these factors are discussed in SI-4 (3).

3. CONCLUSION

Interaction forces and torques are quantified using continuum-based theories grounded in the observed NC configurations. Defects are created during the formation of the superlattice. At the defect regions (point defect, vacancy, edge dislocations, etc.), the significantly unbalanced forces and torques trigger translational and rotational NC motions, respectively, through which the forces and torques are transmitted to neighboring NCs via chain interactions in a 2D network on the Si_xN_y membrane. The rotational motion is characteristic of particles with anisotropic shapes, and the dynamic feature results from the interparticle forces/torques dominated by ligand interactions. This leads to defect self-healing. Thermal (Brownian) motions can cause an initial perturbation in h between NCs, leading to defect self-elimination processes from metastable conditions. The triggered chain interactions involve oscillations of the forces/torques and corresponding translational/rotational velocities, exhibiting specific frequencies depending on the configurations that the NCs assemble into, such as outer NCs vs inner NCs and defect types. Our findings indicate that the anisotropic nature of NCs introduces intricate torques and rotational motion, affecting the superlattice structures. For cubes, the face-to-face configuration is the most stable rather than the brick-wall configuration. In contrast, the triangle configuration is the most energy-stable configuration for spheres.

These mechanisms are further corroborated and demonstrated by well-calibrated MD simulations that produce realistic NC dynamic responses including diffusivity and ligand conformation. Combined with the continuum-based theory and experimental observations, MD confirms that ligand interactions, especially repulsive steric hindrance forces, are the major driving factors behind defect elimination. The attractive force among ligands accounts for NC motions, such as rotation and contributes to keeping the NCs together as one cluster. Some differences between the experimental observations and predictions can be explained by the effect of membranes, hydrodynamic mobilities, and limitations in the theories and simulations; thus, they do not invalidate our analyses.

Our study has established frameworks to understand translational and rotational NC movements at a level of fundamental interaction forces and torques, providing in-depth insights and external conditions to control defect self-elimination processes. Self-consistency is established by coupling different frameworks across length scales. The combined understanding of (1) membrane effects on NP movements, (2) hydrodynamic mobility as a function of configuration, morphology, and separation, and (3) the coupling of NP energetics and dynamics as a function of morphology will allow one to control the self-assembly processes. The self-consistent framework can be expanded to delineate the interaction forces and torques of polyhedron structures and thus can be employed to develop rational bottom-up fabrication of various electronic devices. Further, the knowledge obtained from defect creation to defect elimination during cluster−cluster attachments can be expanded to demystify OA crystallizations and understand vdW and steric hindrance forces and torques for other anisotropically shaped particles.

4. METHODS

4.1. Synthesis of Palladium Nanocube (Pd Cube). Potassium bromide (KBr, ≥ 99%), palladium(II) chloride ($PdCl_2$, ≥99.9%), ethylene glycol (≥99%, EG), 1-dodecanethiol (≥98%), and toluene (≥99.5%) were purchased from Aldrich and Sigma-Aldrich. Polyvinylpyrrolidone (Mn = 40 000 g/mol) (PVP) was purchased from Sigma-Aldrich. Palladium nanocubes were synthesized based on our previous method.[48] These materials were used without further purification. Nine ml of a 12.5 mM $PdCl_2$ aqueous solution was mixed with 1 mL of EG. Then, 0.111 g of PVP and 0.84 mmol of KBr were added to this solution with stirring. After 1 hour, all chemicals were dissolved in a water/EG solution completely. This solution was transferred into a Teflon-lined stainless-steel autoclave (23 mL). The oven was preheated to 160 °C, and the autoclave was put in the oven and maintained at that temperature for 4 hours. The autoclave was taken out of the oven after 4 hours and cooled to room temperature. The solution was transferred to a 1-neck flask. Then, 10 mL of EG was added. The neck flask with solution was heated to 100 °C with an oil bath. Immediately after the solution reached 100 °C, 0.2 mL of 1-dodecanethiol was injected. After 5 min, the neck flask with solution was taken out of the oil bath and cooled to room temperature. The product was collected by centrifugation and washed twice with ethanol and acetone to

https://doi.org/10.1021/acsnano.3c08610
ACS Nano 2024, 18, 32386−32400

remove residual EG, water, and excess 1-dodecanethiol. Finally, the Pd nanocubes were dispersed in toluene (10 mL).

4.2. Preparation of Liquid Cells with Nanocube Solutions. In situ TEM experiments were carried out with a Thermofisher Tecnai microscope at 200 keV. TEM liquid cell chips were purchased from Hummingbird. The electron beam window is an ∼50 nm thick Si_3N_4 membrane. The liquid cells consisted of a 500 nm thick spacer to attain sufficient space for the unconstrained movement of nanocubes. Four μL of as-synthesized Pd nanocubes were introduced to a liquid cell sealed by O-rings for in situ TEM experiments. The assembled liquid cell, including the solution, was placed in a Hummingbird in situ liquid cell TEM holder. The electron dose rate was 8400 e/nm^{2}s. The Direct Detection Device camera from Direct Electron was used for collecting images at a rate of 10 frames per second.

4.3. Characterization of Ligand Concentration Using Thermal Gravimetric Analysis. The weight ratio of the organic compound to the Pd nanocube was investigated by thermal gravimetric analysis (TGA). The dried Pd nanocube samples were mounted on the TGA pan (initial weight: 30 mg). TGA (TMA 402F1, NETZSCH) was conducted in helium by heating the sample from room temperature to 600 °C at a rate of 10 °C/min. The 30 mg of pure 1-dodecanethiol was performed using the same procedure with Pd nanocube TGA analysis.

4.4. Atomistic Simulations. All MD simulations were conducted using the LAMMPS package.[43] An explicit-atom model was applied to represent ligand-coated Pd cubes (see SI-3 for detailed information). The ligand−ligand interactions were described by the interatomic potentials developed by Paul et al.,[37] and the Pd−Pd interactions were described by a Lennard-Jones (LJ) potential developed for face-centered-cubic metals by Heinz et al.[49] The Pd-ligand bonded interactions were developed by our own density functional theory (DFT) simulations using the Vienna Ab Initio Simulation Package (VASP).[50,51] The core electrons were represented using projector-augmented-wave pseudopotentials,[52,53] and the generalized gradient approximation Perdew−Burke−Ernzerhof exchange-correlation functional was used.[54] A universal cutoff of 300 eV was used for all simulations, and the convergence threshold was set to 10^{-6} eV.

ASSOCIATED CONTENT

Supporting Information

The Supporting Information is available free of charge at https://pubs.acs.org/doi/10.1021/acsnano.3c08610.

In situ TEM movie analysis procedures; theoretical calculation of interaction forces between particles; classical molecular dynamics simulations (PDF)

Movie S1. In situ liquid phase TEM full-size movie of the defect self-elimination processes without cropping. The movie play rate is 10× real time (MP4)

Movie S2. In situ liquid phase TEM movie described in Figure 3. The movie play rate is 10× real time (MP4)

Movie S3. In situ liquid phase TEM movie described in Figure 4. The movie play rate is 10× real time (MP4)

Movie S4. In situ liquid phase TEM movie described in Figure 5. The movie play rate is 10× real time (MP4)

Movie S5. In situ liquid phase TEM movie described in Figure 6. The movie play rate is 10× real time (MP4)

Movie S6. In situ liquid phase TEM movie described in Figure 7. The movie play rate is 10× real time (MP4)

Movie S7. In situ liquid phase TEM movie described in Figure 8. The movie play rate is 10× real time (MP4)

AUTHOR INFORMATION

Corresponding Authors

Jaehun Chun − *Physical and Computational Sciences Directorate, Pacific Northwest National Laboratory, Richland, Washington 99352, United States; Levich Institute and Department of Chemical Engineering, CUNY City College of New York, New York, New York 10031, United States;* orcid.org/0000-0002-2291-6496; Email: Jaehun.chun@pnnl.gov

Dongsheng Li − *Physical and Computational Sciences Directorate, Pacific Northwest National Laboratory, Richland, Washington 99352, United States; Levich Institute and Department of Chemical Engineering, CUNY City College of New York, New York, New York 10031, United States; Department of Chemistry, Wayne State University, Detroit, Michigan 48202, United States;* orcid.org/0000-0002-1030-146X; Email: Dongsheng.li2@pnnl.gov

Authors

Jaewon Lee − *Physical and Computational Sciences Directorate, Pacific Northwest National Laboratory, Richland, Washington 99352, United States; Department of Mechanical and Aerospace Engineering and MU Materials Science and Engineering Institute, University of Missouri, Columbia, Missouri 65211, United States;* orcid.org/0000-0002-3434-5707

Zexi Lu − *Physical and Computational Sciences Directorate, Pacific Northwest National Laboratory, Richland, Washington 99352, United States;* orcid.org/0000-0002-8343-9902

Zhigang Wu − *Physical and Computational Sciences Directorate, Pacific Northwest National Laboratory, Richland, Washington 99352, United States; School of Chemistry and Chemical Engineering, North University of China, Taiyuan 030051, PR China*

Colin Ophus − *The National Center for Electron Microscopy, Molecular Foundry, Lawrence Berkeley National Laboratory, Berkeley, California 94720, United States*

Gregory K. Schenter − *Physical and Computational Sciences Directorate, Pacific Northwest National Laboratory, Richland, Washington 99352, United States*

James J. De Yoreo − *Physical and Computational Sciences Directorate, Pacific Northwest National Laboratory, Richland, Washington 99352, United States; Department of Materials Science and Engineering, University of Washington, Seattle, Washington 98195, United States;* orcid.org/0000-0002-9541-733X

Complete contact information is available at: https://pubs.acs.org/10.1021/acsnano.3c08610

Author Contributions

◆J.L., Z.L., and Z.W. contributed equally to this work; Each author's contribution(s) to the paper should be listed; Synthesis of Pd NCs: Z.W., J.L.; In situ TEM experiments: J.L., D.L.; Continuum theory-based calculations: J.L., G.K.S., J.C.; Molecular dynamics simulation: Z.L.; Imaging processing: C.O., J.L.; Data interpretation and discussion: J.L., Z.L., J.C.,

https://doi.org/10.1021/acsnano.3c08610
ACS Nano 2024, 18, 32386−32400

G.K.S., J.J.D.Y., D.L.; Supervision: D.L.; Writing-original draft: J.L., Z.L.; Writing-review and editing: D.L., J.C., G.K.S., J.J.D.Y.

Notes

The work has been previously submitted to a preprint server as below. Jaewon Lee, Zexi Lu, Zhigang Wu, Colin Ophus, Gregory K. Schenter, James J. De Yoreo, Jaehun Chun, Dongsheng Li; Defect Self-Elimination in Nanocube Superlattices through the Interplay of Brownian, van der Waals, and Ligand-Based Forces and Torques. 2023, 10.26434. ChemRxiv, https://chemrxiv.org/engage/chemrxiv/article-details/64f02ce9dd1a73847fdda24c. (September 04, 2023)

The authors declare no competing financial interest.

ACKNOWLEDGMENTS

MD simulations and development of the methodology for extracting forces from TEM data were supported by the U.S. Department of Energy (DOE) Office of Science, Basic Energy Sciences (BES) program, Division of Materials Sciences and Engineering, Synthesis and Processing Sciences Program, FWP 67554. Synthesis of Pd cube particles, development of TEM methods, collection of data on particle assembly, and initial TEM data analysis were supported by Early Career Research program under Award FWP-67037. Theoretical calculations of forces were supported by the Division of Chemical, Bioengineering, Environmental, and Transport Systems, National Science Foundation, under grant CBET-2132355. Hydrodynamic resistivity calculations were supported by the DOE Office of Science, Basic Energy Sciences program, Division of Chemical Sciences, Geosciences and Biosciences, FWP 16249.

ABBREVIATIONS

NC, nanocube; NP, nanoparticle; vdW, van der Waals; LP-TEM, in situ liquid phase transmission electron microscope; F_{vdW}, van der Waals force; τ_{vdW}, van der Waals torque; F_{Sh}, steric hindrance force; τ_{Sh}, steric hindrance torque; F_{Br}, Brownian force; τ_{Br},, Brownian torque; h, interparticle separation; F, interaction forces; τ, interaction torques; θ, rotational angle; F_{Lg}, ligand interaction forces; f, oscillation frequency; υ, velocity; ω, angular velocity; L_g, ligand length in toluene; OA, oriented attachment; CW, clockwise; CCW, counterclockwise

REFERENCES

(1) Boles, M. A.; Engel, M.; Talapin, D. V. Self-assembly of colloidal nanocrystals: From intricate structures to functional materials. *Chem. Rev.* **2016**, *116* (18), 11220−11289.

(2) Talapin, D. V.; Murray, C. B. PbSe nanocrystal solids for n-and p-channel thin film field-effect transistors. *Science* **2005**, *310* (5745), 86−89.

(3) Kim, T.-H.; Chung, D.-Y.; Ku, J.; Song, I.; Sul, S.; Kim, D.-H.; Cho, K.-S.; Choi, B. L.; Kim, J. M.; Hwang, S.; et al. Heterogeneous stacking of nanodot monolayers by dry pick-and-place transfer and its applications in quantum dot light-emitting diodes. *Nat. Commun.* **2013**, *4* (1), 2637.

(4) Gao, Y.; Aerts, M.; Sandeep, C. S.; Talgorn, E.; Savenije, T. J.; Kinge, S.; Siebbeles, L. D.; Houtepen, A. J. Photoconductivity of PbSe quantum-dot solids: Dependence on ligand anchor group and length. *ACS Nano* **2012**, *6* (11), 9606−9614.

(5) Finefrock, S. W.; Zhu, X.; Sun, Y.; Wu, Y. Flexible prototype thermoelectric devices based on Ag 2 Te and PEDOT: PSS coated nylon fibre. *Nanoscale* **2015**, *7* (13), 5598−5602.

(6) Choi, H.; Kim, S.; Kang, S. O.; Ko, J.; Kang, M. S.; Clifford, J. N.; Forneli, A.; Palomares, E.; Nazeeruddin, M. K.; Grätzel, M. Stepwise cosensitization of nanocrystalline TiO2 films utilizing Al2O3 layers in dye-sensitized solar cells. *Angew. Chem., Int. Ed.* **2008**, *47* (43), 8259−8263.

(7) Lee, J.; Zhu, H.; Yadav, G. G.; Caruthers, J.; Wu, Y. Porous ternary complex metal oxide nanoparticles converted from core/shell nanoparticles. *Nano Res.* **2016**, *9* (4), 996−1004.

(8) Kim, F.; Kwan, S.; Akana, J.; Yang, P. Langmuir− Blodgett nanorod assembly. *J. Am. Chem. Soc.* **2001**, *123* (18), 4360−4361.

(9) Collier, C.; Saykally, R.; Shiang, J.; Henrichs, S.; Heath, J. Reversible tuning of silver quantum dot monolayers through the metal-insulator transition. *Science* **1997**, *277* (5334), 1978−1981.

(10) Yang, J.; Choi, M. K.; Kim, D. H.; Hyeon, T. Designed assembly and integration of colloidal nanocrystals for device applications. *Adv. Mater.* **2016**, *28* (6), 1176−1207.

(11) Lee, J.; Nakouzi, E.; Song, M.; Wang, B.; Chun, J.; Li, D. Mechanistic Understanding of the Growth Kinetics and Dynamics of Nanoparticle Superlattices by Coupling Interparticle Forces from Real-Time Measurements. *ACS Nano* **2018**, *12* (12), 12778−12787.

(12) Juárez, J. J.; Feicht, S. E.; Bevan, M. A. Electric field mediated assembly of three dimensional equilibrium colloidal crystals. *Soft Matter* **2012**, *8* (1), 94−103.

(13) Hanrath, T.; Choi, J. J.; Smilgies, D.-M. Structure/processing relationships of highly ordered lead salt nanocrystal superlattices. *ACS Nano* **2009**, *3* (10), 2975−2988.

(14) Juárez, J. J.; Bevan, M. A. Feedback controlled colloidal self-assembly. *Adv. Funct. Mater.* **2012**, *22* (18), 3833−3839.

(15) Lu, F.; Yager, K. G.; Zhang, Y.; Xin, H.; Gang, O. Superlattices assembled through shape-induced directional binding. *Nat. Commun.* **2015**, *6*, 6912.

(16) Choi, J. J.; Bian, K.; Baumgardner, W. J.; Smilgies, D.-M.; Hanrath, T. Interface-induced nucleation, orientational alignment and symmetry transformations in nanocube superlattices. *Nano Lett.* **2012**, *12* (9), 4791−4798.

(17) Bishop, K. J.; Wilmer, C. E.; Soh, S.; Grzybowski, B. A. Nanoscale forces and their uses in self-assembly. *Small* **2009**, *5* (14), 1600−1630.

(18) Nakouzi, E.; Soltis, J. A.; Legg, B. A.; Schenter, G. K.; Zhang, X.; Graham, T. R.; Rosso, K. M.; Anovitz, L. M.; De Yoreo, J. J.; Chun, J. Impact of solution chemistry and particle anisotropy on the collective dynamics of oriented aggregation. *ACS Nano* **2018**, *12* (10), 10114−10122.

(19) Xiao, D.; Wu, Z.; Song, M.; Chun, J.; Schenter, G. K.; Li, D. Silver nanocube and nanobar growth via anisotropic monomer addition and particle attachment processes. *Langmuir* **2018**, *34* (4), 1466−1472.

(20) Roth, C. M.; Neal, B. L.; Lenhoff, A. M. Van der Waals interactions involving proteins. *Biophys. J.* **1996**, *70* (2), 977−987.

(21) Kaushik, A. P.; Clancy, P. Explicit all-atom modeling of realistically sized ligand-capped nanocrystals. *J. Chem. Phys.* **2012**, *136* (11), 114702.

(22) Kaushik, A. P.; Clancy, P. Solvent-driven symmetry of self-assembled nanocrystal superlatticesA computational study. *J. Comput. Chem.* **2013**, *34* (7), 523−532.

(23) Plimpton, S. Computational limits of classical molecular dynamics simulations. *Comput. Mater. Sci.* **1995**, *4* (4), 361−364.

(24) Li, D.; Chun, J.; Xiao, D.; Zhou, W.; Cai, H.; Zhang, L.; Rosso, K. M.; Mundy, C. J.; Schenter, G. K.; De Yoreo, J. J. Trends in mica−mica adhesion reflect the influence of molecular details on long-range dispersion forces underlying aggregation and coalignment. *Proc. Natl. Acad. Sci. U. S. A.* **2017**, *114* (29), 7537−7542.

(25) de Graaf, J.; van Roij, R.; Dijkstra, M. Dense regular packings of irregular nonconvex particles. *Phys. Rev. Lett.* **2011**, *107* (15), 155501.

(26) Damasceno, P. F.; Engel, M.; Glotzer, S. C. Predictive self-assembly of polyhedra into complex structures. *Science* **2012**, *337* (6093), 453−457.

(27) Gong, J.; Newman, R. S.; Engel, M.; Zhao, M.; Bian, F.; Glotzer, S. C.; Tang, Z. Shape-dependent ordering of gold nanocrystals into large-scale superlattices. *Nat. Commun.* **2017**, *8* (1), 14038.

https://doi.org/10.1021/acsnano.3c08610
ACS Nano 2024, 18, 32386−32400

(28) Smallenburg, F.; Filion, L.; Marechal, M.; Dijkstra, M. Vacancy-stabilized crystalline order in hard cubes. *Proc. Natl. Acad. Sci. U. S. A.* **2012**, *109* (44), 17886−17890.
(29) Soligno, G.; Dijkstra, M.; van Roij, R. Self-assembly of cubes into 2D hexagonal and honeycomb lattices by hexapolar capillary interactions. *Phys. Rev. Lett.* **2016**, *116* (25), 258001.
(30) Gantapara, A. P.; de Graaf, J.; van Roij, R.; Dijkstra, M. Phase diagram and structural diversity of a family of truncated cubes: Degenerate close-packed structures and vacancy-rich states. *Phys. Rev. Lett.* **2013**, *111* (1), 015501.
(31) Singh, G.; Chan, H.; Baskin, A.; Gelman, E.; Repnin, N.; Král, P.; Klajn, R. Self-assembly of magnetite nanocubes into helical superstructures. *Science* **2014**, *345* (6201), 1149−1153.
(32) Henzie, J.; Grünwald, M.; Widmer-Cooper, A.; Geissler, P. L.; Yang, P. Self-assembly of uniform polyhedral silver nanocrystals into densest packings and exotic superlattices. *Nat. Mater.* **2012**, *11* (2), 131.
(33) Quan, Z.; Xu, H.; Wang, C.; Wen, X.; Wang, Y.; Zhu, J.; Li, R.; Sheehan, C. J.; Wang, Z.; Smilgies, D.-M.; et al. Solvent-mediated self-assembly of nanocube superlattices. *J. Am. Chem. Soc.* **2014**, *136* (4), 1352−1359.
(34) Li, F.; Delo, S. A.; Stein, A. Disassembly and Self-Reassembly in Periodic Nanostructures: A Face-Centered-to-Simple-Cubic Transformation. *Angew. Chem., Int. Ed.* **2007**, *46* (35), 6666−6669.
(35) Li, R.; Bian, K.; Wang, Y.; Xu, H.; Hollingsworth, J. A.; Hanrath, T.; Fang, J.; Wang, Z. An obtuse rhombohedral superlattice assembled by Pt nanocubes. *Nano Lett.* **2015**, *15* (9), 6254−6260.
(36) Wang, T.; Wang, X.; LaMontagne, D.; Wang, Z.; Wang, Z.; Cao, Y. C. Shape-controlled synthesis of colloidal superparticles from nanocubes. *J. Am. Chem. Soc.* **2012**, *134* (44), 18225−18228.
(37) Paul, W.; Yoon, D. Y.; Smith, G. D. An optimized united atom model for simulations of polymethylene melts. *J. Chem. Phys.* **1995**, *103* (4), 1702−1709.
(38) Wick, C. D.; Martin, M. G.; Siepmann, J. I. Transferable potentials for phase equilibria. 4. United-atom description of linear and branched alkenes and alkylbenzenes. *J. Phys. Chem. B* **2000**, *104* (33), 8008−8016.
(39) Maeda, H.; Maeda, Y. Orientation-Dependent London−van der Waals Interaction Energy between Macroscopic Bodies. *Langmuir* **2015**, *31* (26), 7251−7263.
(40) Halperin, A.; Tirrell, M.; Lodge, T. Tethered Chains in Polymer Microstructures. In *Macromolecules: Synthesis, Order and Advanced Properties*; Springer, 1992; pp. 31−71.
(41) Murray, C. B.; Kagan, C. R.; Bawendi, M. G. Synthesis and characterization of monodisperse nanocrystals and close-packed nanocrystal assemblies. *Annu. Rev. Mater. Sci.* **2000**, *30* (1), 545−610.
(42) Li, D.; Nielsen, M. H.; Lee, J. R. I.; Frandsen, C.; Banfield, J. F.; De Yoreo, J. J. Direction-specific interactions control crystal growth by oriented attachment. *Science* **2012**, *336* (6084), 1014−1018.
(43) Plimpton, S. Fast parallel algorithms for short-range molecular dynamics. *J. Comput. Phys.* **1995**, *117* (1), 1−19.
(44) Keim, P.; Maret, G.; Herz, U.; von Grünberg, H. H. Harmonic Lattice Behavior of Two-Dimensional Colloidal Crystals. *Phys. Rev. Lett.* **2004**, *92* (21), 215504.
(45) De Gennes, P. Polymers at an Interface; a Simplified View. *Adv. Colloid Interface Sci.* **1987**, *27* (3−4), 189−209.
(46) McLachlan, A. Van der Waals forces between an atom and a surface. *Mol. Phys.* **1964**, *7* (4), 381−388.
(47) Jeffrey, D.; Onishi, Y. Calculation of the Resistance and Mobility Functions for Two Unequal Rigid Spheres in Low-reynolds-number Flow. *J. Fluid Mech.* **1984**, *139*, 261−290.
(48) Wu, Z.; Xiao, D.; Lee, J.; Ren, P.; Song, M.; Li, D. Palladium nanostructures with well-controlled morphologies obtained by one-pot and one-step polyol method. *J. Cryst. Growth* **2019**, *521*, 34−40.
(49) Heinz, H.; Vaia, R.; Farmer, B.; Naik, R. Accurate simulation of surfaces and interfaces of face-centered cubic metals using 12− 6 and 9− 6 Lennard-Jones potentials. *J. Phys. Chem. C* **2008**, *112* (44), 17281−17290.
(50) Kresse, G.; Hafner, J. Ab initio molecular dynamics for liquid metals. *Phys. Rev. B* **1993**, *47* (1), 558−561.
(51) Kresse, G.; Furthmuller, J. Efficiency of ab-initio total energy calculations for metals and semiconductors using a plane-wave basis set. *Comput. Mater. Sci.* **1996**, *6* (1), 15−50.
(52) Blochl, P. E. Projector Augmented-Wave Method. *Phys. Rev. B* **1994**, *50* (24), 17953−17979.
(53) Kresse, G.; Joubert, D. From ultrasoft pseudopotentials to the projector augmented-wave method. *Phys. Rev. B* **1999**, *59* (3), 1758−1775.
(54) Perdew, J. P.; Burke, K.; Ernzerhof, M. Generalized gradient approximation made simple. *Phys. Rev. Lett.* **1996**, *77* (18), 3865−3868.

https://doi.org/10.1021/acsnano.3c08610
ACS Nano 2024, 18, 32386−32400